Two Disease-Causing SNAP-25B Mutations Selectively Impair SNARE C-terminal Assembly

Aleksander A. Rebane[a,b,c], **Bigeng Wang**[a,1], **Lu Ma**[a], **Sarah M. Auclair**[a], **Hong Qu**[a], **Jeff Coleman**[a], **Shyam Krishnakumar**[a], **James E. Rothman**[a,*], and **Yongli Zhang**[a,*]

[a]Department of Cell Biology, Yale School of Medicine, New Haven, CT 06511, USA

[b]Integrated Graduate Program in Physical and Engineering Biology

[c]Department of Physics, Yale University, New Haven, CT 06511, USA

[1]Current address: Department of Physics, Columbia University, New York, NY 10027, USA

*Correspondence: james.rothman@yale.edu, yongli.zhang@yale.edu

KEYWORDS

Optical tweezers, SNARE assembly, membrane fusion, protein folding, neuropathy

ABSRACT

Synaptic exocytosis relies on assembly of three soluble N-ethylmaleimide-sensitive factor attachment protein receptor (SNARE) proteins into a parallel four-helix bundle to drive membrane fusion. SNARE assembly occurs by step-wise zippering of the vesicle-associated SNARE (v-SNARE) onto a binary SNARE complex on the target plasma membrane (t-SNARE). Zippering begins with slow N-terminal association followed by rapid C-terminal zippering, which serves as a power stroke to drive membrane fusion. SNARE mutations have been associated with numerous diseases, including neurological disorders. It remains unclear how these mutations affect SNARE zippering, partly due to difficulties to quantify the energetics and kinetics of SNARE assembly. Here, we used single-molecule optical tweezers to measure the assembly energy and kinetics of SNARE complexes containing single mutations I67T/N in neuronal SNARE synaptosomal-associated protein of 25 kDa (SNAP-25B), which disrupt neurotransmitter release and have been implicated in neurological disorders. We found that both mutations significantly reduced the energy of C-terminal zippering by ~10 k_BT, but did not affect N-terminal assembly. In addition, we observed that both mutations lead to unfolding of the C-terminal region in the t-SNARE complex. Our findings suggest that both SNAP-25B mutations impair synaptic exocytosis by destabilizing SNARE assembly, rather than stabilizing SNARE assembly as previously proposed. Therefore, our measurements provide insights into the molecular mechanism of the disease caused by SNARE mutations.

HIGHLIGHTS

- The mechanism by which two SNAP-25B mutations cause disease is unclear.
- The mutations greatly weaken SNARE C-terminal zippering.

- The mutations do not affect SNARE N-terminal assembly.
- The mutations impair t-SNARE folding.
- The mutations impair SNARE assembly and thus lead to impaired neurotransmission.

Abbreviations

SNARE – soluble N-ethylmaleimide-sensitive factor attachment protein receptors

VAMP2 – vesicle-associated membrane protein 2

SNAP-25 – synaptosomal-associated protein of molecular weight 25 kDa

v-SNARE – vesicle-associated SNARE

t-SNARE – target membrane-associated SNARE

NTD – N-terminal domain of the SNARE complex

CTD – C-terminal domain of the SNARE complex

LD – linker domain of the SNARE complex

FEC – Force-extension curve

HMM – Hidden Markov modeling

Glossary

Ternary complex – SNARE complex comprising VAMP2, SNAP-25, and syntaxin that exhibits a four-helix coiled-coil structure.

t-SNARE complex – Partially structured SNARE complex comprising SNAP-25 and syntaxin located on the target membrane.

***trans*-SNARE**– Partially assembled ternary SNARE complex where complementary v- and t-SNAREs bridge two membranes in *trans*. This intermediate is formed by vesicle priming and

acts as a precursor to the final fusion step.

Layers – Buried, inward-facing amino acid residues between helices in the four-helix bundle structure of the SNARE complex numbered from -7 to +8 from the N-terminus to C-terminus. The residues in the 0 layer are either glutamine or arginine, whereas residues in other layers are hydrophobic.

Equilibrium force – Force at which a two-state transition exhibits 50% unfolding probability.

Equilibrium transition rate – Transition rate at equilibrium force, where folding and unfolding rates are equal.

INTRODUCTION

Intracellular trafficking and secretion relies on *s*oluble *N*-ethylmaleimide-sensitive factor *a*ttachment protein *re*ceptors (SNAREs) to fuse cargo-containing vesicles to target membranes [1, 2]. Complementary SNAREs are C-terminally anchored to the vesicles (v-SNARE) or the target membranes (t-SNARE) [3]. In the case of synaptic vesicle exocytosis, the v-SNARE consists of the *v*esicle-*a*ssociated *m*embrane protein 2 (VAMP2) and the t-SNARE comprises a partially structured binary complex of 25 kDa *s*ynaptosomal-*a*ssociated *p*rotein B (SNAP-25B) and syntaxin 1A [4-8]. When in proximity, v- and t-SNAREs zipper from their N-terminal to C-terminal ends to form a stable four-helix bundle, contributing one and three helices, respectively (Fig. 1) [9-12]. Energy that is released during SNARE assembly lowers the energy barrier posed by membrane-membrane repulsion and thereby accelerates the fusion process. The tight association of the four-helix bundle is mediated by 15 layers of hydrophobic amino acids (numbered from -7 to +8) and a central ionic layer ("0" layer) in the core of the bundle [13]. Point mutations that disrupt these hydrophobic layers in the N-terminal domain (Figure 1, NTD)

or C-terminal domain (CTD) impair vesicle docking at the plasma membrane and Ca^{2+}-triggered membrane fusion, respectively [10, 14, 15]. Therefore, assembly of each SNARE domain corresponds to a distinct stage in synaptic exocytosis with unique function.

SNARE mutations have been implicated in various diseases or disorders, including neurological disorders, cancer, immunodeficiency, and diabetes [16-20]. Particularly, SNARE mutations have been identified in patients with congenital myasthenic syndrome, a group of inherited diseases of the neuromuscular junction that are characterized by fatigable muscle weakness [21-23]. In two cases of interest, the dominant disease-causing mutation affects codon 67 of SNAP-25B, which lies in the +4 hydrophobic layer of the SNARE CTD (Fig. 1). In the first case, a human patient carrying the SNAP-25B mutation I67N suffers from myasthenia, cerebellar ataxia, cortical hyperexcitability, and intellectual disability [21]. Transfected into bovine chromaffin cells, the mutant SNAP-25B impairs evoked exocytosis. In the second case, SNAP-25B I67T was identified in the blind-drunk mouse [16]. The mouse exhibits ataxic gait at around 4 weeks of age, as well as impaired sensorimotor gating, an important component of the schizophrenia phenotype related to altered sensory processing. Transfected into murine cortical brain cells and pancreatic beta-cells, the I67T mutant impaired both constitutive and evoked exocytosis, with markedly reduced replenishment of the readily releasable pool of vesicles. Surprisingly, *in silico* modeling and melting temperature measurements of the mutant SNARE complex suggest that the mutation I67T stabilized the SNARE four-helix bundle. Consequently, the mutation was expected to facilitate, not impair membrane fusion, since more energy is released during SNARE assembly to drive exocytosis. Thus, it remains controversial how the two SNAP-25B mutations impair synaptic transmission.

SNARE assembly is difficult to study using traditional bulk assays. The experimental challenge is to resolve the multiple intermediates of SNARE assembly under conditions that mimic membrane fusion in the presence of force, and to minimize misfolding of the SNARE complexes [11, 12, 24, 25]. We have developed a high-resolution optical tweezers approach to apply precisely known pulling forces on a single cytosolic SNARE complex molecule to mimic membrane repulsion during membrane fusion, while observing its folding/unfolding in real-time, on sub-millisecond timescale and at sub-nanometer resolution [15, 26-29]. These time-resolved force-extension measurements have yielded the assembly energetics and kinetics of SNARE cytosolic domain, along with the structures of key folding intermediates [12, 15, 25]. We have identified at least three stages of synaptic ternary SNARE assembly - NTD, CTD, and the linker domain (LD) - and found that CTD stability is particularly sensitive to mutations in its hydrophobic layers +4 to +6 [12, 15]. Thus, the energy released during CTD assembly can serve as the power stroke that drives membrane fusion [30]. In this work, we hypothesized that the SNAP-25B mutations I67N and I67T cause the synaptic malfunction by impairing SNARE assembly. To test the hypothesis, we used optical tweezers to measure the assembly energetics and kinetics of both complexes with mutant SNAP-25B. We find that the mutants greatly destabilized the ternary complex CTD without affecting the NTD, and disrupted the partially structured C-terminal portion of the t-SNARE binary complex.

RESULTS

SNAP-25B Mutations Destabilize SNARE CTD

To study SNARE assembly, we tethered single cytosolic SNARE complexes between two polystyrene beads trapped in two tightly focused laser beams and pulled the complexes by

129 separating the two optical traps (Fig. 1) [12, 29]. On one side of the complex, the VAMP2 C-
130 terminus was attached to an anti-digoxigenin-coated bead via a digoxigenin-functionalized 2,260
131 bp DNA handle [31]. On the other side, the syntaxin C-terminus was biotinylated using an Avi-
132 tag and directly attached to a streptavidin-coated bead. To facilitate SNARE refolding, we cross-
133 linked VAMP2 and syntaxin with a disulfide bridge at their N-termini (-6 layer) [15]. We applied
134 force on the tethered molecule by controlling the distance between the two optical traps and
135 simultaneously measured the tether extension by monitoring bead displacements from the trap
136 centers [27, 28]. The SNAREs were fully assembled when the tether was initially formed. We
137 then pulled and subsequently relaxed the SNARE complex by gradually increasing and
138 decreasing the trap separation, respectively. Figure 2a shows the resulting force-extension curves
139 (FECs) for WT and SNAP-25B mutants I67T/N, with black and cyan curves corresponding to
140 the pulling and relaxation phases, respectively. FECs comprise continuous stretches (fit by red
141 curves), regions of extension flickering, and discrete extension jumps (gray arrow). Continuous
142 signals stem from elastic stretching of both the DNA handle and any unfolded polypeptides [32],
143 while the protein remains in a single folding state (indicated by the corresponding state number).
144 Flickering represents reversible protein unfolding/refolding transitions between two or more
145 discrete states [33]. Lastly, jumps in the signal indicate irreversible unfolding/refolding
146 transitions between states that are separated by a high energy barrier and cannot reach
147 thermodynamic equilibrium during pulling or relaxation.

148 The WT SNARE complex (in state 1) disassembled in three reversible and one
149 irreversible steps (Figs. 2a & b). The first transition between states 1 and 2 occurred at an
150 equilibrium force of 11.6 (±0.6, standard deviation, N=29) pN and represents reversible
151 unfolding/refolding of the LD. The subsequent transition between states 2 and 3 at 16.5 (±0.8,

N=90) pN stemmed from the folding and unfolding of the CTD. The last transition between states 3 and 4 at 17.2 (±0.8, N=73) pN was associated with the NTD. Pulled to even higher force, the SNARE underwent an irreversible transition from state 4 to 5 as SNAP-25B dissociated from the t-SNARE complex. The remaining unfolded SNAREs could not refold even after relaxing to low force. Thus, the LD, CTD, and NTD in the WT complex exhibited distinct stabilities, with the CTD unfolding at significantly greater force than the LD. All these measurements on the WT SNARE complex are consistent with previous reports [12, 15, 30].

In contrast, both SNAP-25B mutants unfolded in only two reversible steps. In both cases, the intermediate state 2 (LD unfolded four-helix bundle state) disappeared and the LD and the CTD folded and unfolded as a single unit at considerably lower force than the WT CTD, but close to the WT LD. We measured equilibrium force 12.0 (±0.5, N=15) pN for I67T and 10.5 (±0.8, N=37) pN for I67N (Fig. 2a). These measurements suggest that both SNAP-25B mutations significantly destabilized the CTD. Consequently, the CTD now exhibited similar (for I67T) or even lower (for I67N) mechanical stability than the LD, leading to simultaneous folding and unfolding transitions of both domains. However, the NTDs in both mutants unfolded at forces equal to WT within experimental error, with equilibrium force of 17.0 (±0.7, N=14) pN for I67T and 16.8 (±0.8, N=30) pN for I67N. In summary, the FECs show that both mutations specifically destabilized the CTD of the four-helix bundle while leaving the NTD unaffected.

Quantification of SNARE Zippering Energetics, Kinetics, and Intermediates

To quantify the energetics and kinetics of the mutant SNARE complexes, we measured a series of extension trajectories at distinct trap separations or mean forces. The forces were chosen so as to sample the entire force region where the transition occurred. Figure 3 shows

175 excerpts from typical extension trajectories of the LD/CTD transition in I67T and I67N mutants,
176 as well as the CTD transition in WT SNARE complexes (black traces). To verify the two-state
177 nature of the transitions, we plotted the probability density distributions of the extensions and
178 found that double-Gaussian functions fit the bimodal distributions well (green curves). The
179 extension fluctuation around each peak was mainly caused by Brownian motion of the trapped
180 beads [34]. The area below each Gaussian function represents the probability of the
181 corresponding state. An increase in force led to an increase in the unfolding probability, as is
182 expected for typical force-induced two-state transitions under equilibrium conditions [26, 35].
183 Besides a reduction in equilibrium force, both mutations slowed down the folding and unfolding
184 processes. Thus, we conclude that the SNAP-25B mutations not only destabilize the CTD, but
185 also slow down CTD zippering.

186 We used hidden Markov modeling (HMM) to derive the state transitions underlying each
187 extension trajectory obscured by noise (Materials and Methods) [34]. HMM yielded noise-free
188 idealized transitions (Fig. 3, red traces), which closely match the corresponding extension
189 trajectories. Furthermore, HMM revealed the average state extensions and forces, as well as the
190 unfolding probabilities and folding/unfolding rates. The force-dependent unfolding probabilities
191 follow a sigmoidal curve (Fig. 4a, upper panel), similar to that seen in denaturant-based protein
192 folding experiments, with force acting a similar role as the denaturant [36, 37]. Similarly,
193 logarithms of the force-dependent unfolding rates (lower panel, solid symbols) and folding rates
194 (hollow symbols) increase and decrease approximately exponentially in the force region tested,
195 respectively. We were able to accurately determine SNARE zippering kinetics from extensive
196 measurements on single SNARE complexes (Fig. 4a,b). In addition, results from different
197 molecules were highly consistent (Fig. 4c).

To determine the free energies and conformations of the folded, unfolded, and transition states at zero force, we simultaneously fit the measured unfolding probabilities, transition rates, and extension changes by a non-linear model (Fig. 4a, curves) [35]. The model describes the observed two-state transition in terms of a force-dependent folding energy landscape comprising folded, unfolded, and transition states. This model allows us to calculate the unfolding probability based on the Boltzmann distribution and the folding/unfolding rates according to the Kramers' theory at each force. For each state, we calculated the total energy of the system including the potential energies of two beads in optical traps, entropic energies of the stretched DNA handle and polypeptides, and the intrinsic free energy of the protein at zero force. We described the DNA and unfolded polypeptides using the worm-like chain model (Eq. 3), which relates the polymer's force-dependent extension and entropic energy to the its contour length and flexibility [32]. The DNA contour length is a known experimental parameter (2,260 bp or 768.4 nm), but the contour length of the unfolded polypeptide needs to be determined, since it depends on the folding state of the protein. Thus, our model features two fitting parameters for each state: its free energy at zero force and the contour length of the unfolded, stretched polypeptide. We therefore obtained the energies and polypeptide contour lengths of all states at zero force by fitting the HMM results with model predictions (see Materials and Methods for details). Notably, the model fitting (Fig. 4a, curves) accurately reproduces the experimentally determined HMM results (symbols).

Disease-causing Mutations Differentially Affect NTD and CTD Assembly

Model fitting confirmed that the two-state transitions in I67T and I67N correspond to coupled folding of the CTD (+3 layer to +8 layer) and the LD (+8 layer to cytosolic C-terminus)

[15, 35]. We derived coupled LD/CTD folding energies of 23 (±3) k_BT for I67T and 19 (±3) k_BT for I67N, where k_B is the Boltzmann constant and T the absolute temperature (Fig. 4c, red bars). For WT, we added the folding energies of 25 (±2) k_BT for the CTD and of 8 k_BT (±2) k_BT for the LD, yielding a combined LD/CTD energy of 33 (±3) k_BT. Therefore, the I67T and I67N mutations destabilize the LD/CTD by 10 k_BT and 14 k_BT, respectively. The equilibrium LD/CTD transition rates of I67T (30 s^{-2}) and I67N (10 s^{-2}) were reduced by three-fold and ten-fold, respectively, compared to that of the WT CTD (100 s^{-2}) (Fig. 4a, lower panel). The reconstructed energy landscape at zero force (Fig. 4d) supports this observation. In particular, the mutations give rise to a small energy barrier (0.5 k_BT for I67T and 2 k_BT for I67N) for the LD/CTD transition. These findings demonstrate that the two disease mutations greatly destabilized the LD/CTD.

In contrast to LD and CTD assembly, the SNAP-25B mutations have negligible effect on the NTD. Using the methods introduced above, we determined the force-dependent unfolding probabilities and transition rates for the NTD (Fig. 4b). The mutants have the same equilibrium forces and rates as the WT within experimental error. Model fitting yielded NTD folding energies of 37 (±4) k_BT for I67T, 36 (±3) k_BT for I67N, and 38 (±2) k_BT for WT (Fig. 4c, gray bars). In all cases, NTD folding involved association of VAMP2 with the t-SNARE complex from -6 to +3 layers and faced no energy barrier at zero-force (Fig 4d). In summary, both SNAP-25B mutations only destabilize C-terminal assembly and are therefore expected to selectively impair the fusion step of synaptic exocytosis.

SNAP-25B Mutations Impair t-SNARE Folding

Next, we investigated how the mutations affect the cytosolic t-SNARE complex. In this case, we pulled the t-SNARE complex from the C-terminus of syntaxin and the C-terminus of SN1 domain in SNAP-25B (Fig. 5a), as previously described [38]. The two SNARE proteins were crosslinked at the N-termini of both SNARE domains. To prevent t-SNARE misfolding, we first formed the ternary SNARE complex and then removed the VAMP2 molecule by disassembling the ternary complex *in situ*, generating the unfolded t-SNARE complex (Figs. 5a & b, state ii). Interestingly, even in this new pulling direction, the CTD of the mutant ternary SNARE complex reversibly unfolded at significantly lower force than the WT complex (green arrows), consistent with a weak CTD in the mutants. As the syntaxin-SNAP-25B conjugate was relaxed to around 5 pN, both WT and mutant t-SNAREs reversibly folded into the t-SNARE complex (state 3). Figure 5c shows typical extension trajectories of the mutant and WT t-SNARE folding transitions near equilibrium force (black traces). The mutant t-SNARE complexes exhibit lower equilibrium forces than WT t-SNARE complex, suggesting that the mutations weaken the t-SNARE complex. In addition, the extension change accompanying the folding transition is reduced in the mutants with respect to WT, indicating that the mutant t-SNAREs are less structured than the WT. We then quantified the force-dependent unfolding probabilities and unfolding/refolding rates for this transition using HMM (Fig. 6a, symbols). Model fitting (Fig. 6a, curves) revealed greatly reduced mutant t-SNARE folding energies of 6 (±2) k_BT and 7 (±2) k_BT for I67T and I67N, respectively, compared to 12 (±3) k_BT for WT (Fig 6b). The derived zero-force energy landscape (Fig. 6c) shows that the mutations result in a ~9 k_BT energy barrier near the -3 layer, compared to the ~6 k_BT energy barrier near the +1 layer in WT. The folded states of the mutants are less structured than in WT, with I67T and I67N structured to +1 and +2 layers, respectively, compared to WT, which is structured to +5 layer. Together, these data show

that the mutations disrupt the C-terminal portion of the t-SNARE complex and thereby reduce t-SNARE folding energies by at least 5 k_BT.

DISCUSSION

We used optical tweezers to determine the effect of disease-causing SNAP-25B mutations I67T and I67N on the energetics, kinetics, and intermediates of SNARE complex assembly. To our knowledge, these are the first single-molecule measurements to elucidate the molecular mechanism of disease-causing SNARE mutations. We show that the mutations, which lie in the +4 hydrophobic layer in the CTD, selectively destabilize LD/CTD assembly by at least 10 k_BT (Fig. 4c). Previous studies have demonstrated that mutations that destabilize the C-terminal assembly severely impair Ca^{2+}-triggered membrane fusion [10, 14, 15]. In particular, the +4 layer mutation VAMP2 L70A, which was shown to destabilize LD/CTD assembly by 10 k_BT [15], dramatically reduces Ca^{2+}-triggered neurotransmitter release in chromaffin cells [14]. The equally great destabilization of LD/CTD assembly in the SNAP-25B mutants is therefore expected to strongly inhibit membrane fusion, consistent with the reduced spontaneous and evoked neurotransmitter release observed *in vivo* [16, 21].

NTD assembly mediates vesicle docking and forms the partially assembled *trans*-SNARE intermediate that acts as a precursor to vesicle priming and Ca^{2+}-triggered fusion [2, 12, 14, 15]. We found that the SNAP-25B mutations have no effect on NTD assembly, which suggests that mutant SNAREs can participate in vesicle docking likely as well as their WT counterpart. Furthermore, vesicle docking is mediated by multiple copies of trans-SNARE complexes [39, 40]. Therefore, in cells that express both WT and mutant SNAREs, a docked vesicle should contain equal numbers of WT and mutant *trans*-SNARE complexes on average. It is likely that

289 Ca^{2+}-triggered vesicle fusion is abolished by a single copy of defective trans-SNARE complex in
290 a docked vesicle [15]. Thus, our findings may account for the dominant disease phenotype of
291 both SNAP-25 mutations.

292 The total energy released by assembly of a v-SNARE and preformed t-SNARE into a
293 single ternary SNARE is 60 k_BT for I67T, 55 k_BT for I67N, and 71 k_BT for the WT.
294 Additionally, the energy of t-SNARE formation is 6 k_BT and 7 k_BT for I67T and I67N mutants,
295 respectively, and 12 k_BT for the WT. Thus, the I67T and I67N mutations reduce the total
296 SNARE complex formation energy by 17 k_BT and 20 k_BT, respectively, compared to the WT.
297 Our results contrast with the report by Jeans et al. [16]. Based on an increase in melting
298 temperature for the I67T ternary SNARE, these authors suggest that the mutation increased the
299 thermodynamic stability of the ternary SNARE complex. Consequently, they reasoned that the
300 reduced *in vivo* exocytosis stems from the impaired vesicle recycling, as increased SNARE
301 stability might hinder SNARE disassembly and recycling for subsequent rounds of fusion. We
302 note that SNARE complexes melt far from thermodynamic equilibrium and thus the melting
303 temperature of the SNARE complex mainly represents the energy barrier of SNARE unfolding,
304 instead of thermodynamic stability of the SNARE complex. In contrast, our single-molecule
305 measurement is conducted under thermodynamic equilibrium and yields the free energy of
306 SNARE folding and assembly [25]. We therefore suggest that in addition to impairing the
307 replenishment of the readily releasable pool by a yet unknown mechanism, the SNAP-25B
308 mutations compromise the ternary SNARE's ability to drive membrane fusion. In summary, our
309 findings provide hitherto missing molecular detail on how single SNARE mutations can impair
310 synaptic transmission to a degree that leads to neurological disorders such as congenital
311 myasthenic syndrome.

MATERIALS AND METHODS

SNARE Proteins

We employed the cytosolic domain of mouse VAMP2 (residues 1-96) with a C-terminal linker sequence (GGSGNGSGGLSTPSRGG), followed by a FLAG tag (DYKDDDDK) [12]. For the ternary SNARE complex pulling experiment, we engineered a cysteine via Q36C site-directed mutagenesis (Agilent Technologies) to facilitate crosslinking to syntaxin at the -6 layer [15]. Additionally, to allow covalent attachment to the DNA handle, we mutated a serine in the linker (underlined in the sequence) to a cysteine. The syntaxin construct comprised the cytosolic domain of rat syntaxin 1A (residues 1-265, mutation C145S) with a C-terminal linker sequence (GGSGNGGSGS), followed by an Avi-tag (GLNDIFEAQKIEWHE) [12]. The -6 layer cysteine in syntaxin was added by site-directed mutagenesis L205C [15]. For t-SNARE complex pulling, we instead added a cysteine at the -8 layer by mutating H199C [38]. The VAMP2 and syntaxin genes were cloned into the pET-SUMO vector (Thermo Fisher). For the full-length mouse SNAP-25B, we replaced all intrinsic cysteines with serines (mutations C85S, C88S, C90S, C92S) and inserted it into the pET-28a vector. For the t-SNARE complex pulling experiment, we additionally mutated S25C to facilitate crosslinking to syntaxin at the -8 layer and N93C to allow for covalent attachment of the DNA handle.

We expressed all proteins in BL21 Gold (DE3) cells (Agilent Technologies) and purified the proteins using nickel nitriloacetic acid beads (GE Healthcare Lifesciences) and the buffer containing 25 mM HEPES, 400 mM KCl, 1 mM TCEP, 10 mM imidazole, and 10% glycerol. After purification, we enzymatically biotinylated syntaxin using the biotin ligase BirA (Avidity), leading to biotin conjugation to the underlined lysine in the Avi-tag sequence [29]. For VAMP2

and syntaxin, the N-terminal SUMO protein was cleaved along with the His-tag using SUMO protease. To form the SNARE complex, we mixed syntaxin, SNAP-25B, and VAMP2 at a molar ratio of 1:1:2, followed by an overnight incubation at 4 °C, in the presence of 3 mM Tris(2-carboxyethyl) phosphine (TCEP). Then the SNARE complex was purified using the N-terminal His-tag on SNAP-25B, followed by overnight incubation in the absence of TCEP at 4 °C to allow disulfide bond formation between VAMP2 and syntaxin (for ternary SNARE pulling experiment) or SNAP-25B and syntaxin (for t-SNARE pulling experiment).

High-Resolution Optical Tweezers

We used home-built dual-trap optical tweezers with interferometric detection, as previously described [27, 28]. Briefly, we used a 1064 nm laser beam to form the optical traps. To this end, we expanded, collimated, and then split the beam into two orthogonally polarized beams, each corresponding to one trap. We reflected one beam by a mirror that could be tipped and tilted along two axes with high precision by virtue of a nano-positioning stage (Mad City Labs), thus controlling the beam's path relative to the other. The two beams were subsequently combined and expanded once more, and finally focused by a water-immersion 60X objective with numerical aperture of 1.2 (Olympus) to form two optical traps. The outgoing laser beams were collimated by an identical objective and split again by polarization. The separated beams were each projected onto a position-sensitive detector (Pacific Silicon Sensor) to detect bead displacements from the trap center using back-focal-plane interferometry [41]. The force constants and the constants to convert detector signal to bead displacement were calibrated using the Brownian motion of the trapped beads. The force, bead displacement, trap separation, and other experimental parameters were acquired at 20 kHz, filtered online to 10 kHz and stored on

hard-disc. Importantly, the tether extension was directly calculated by subtracting the bead radii and bead displacements from the trap separation.

Single-Molecule Experiments

We covalently attached a 2,260 bp DNA handle to the C-terminal cysteine on VAMP2 (for ternary complex pulling) or on SNAP-25B (t-SNARE pulling). This was done by mixing the purified SNARE complex with DNA handle at 100:1 molar ratio, as is described in detail elsewhere [29]. The final DNA handle concentration was approximately 150 nM. A 2 μL aliquot of the protein-DNA mixture was incubated with 20 μL anti-digoxigenin antibody-coated polystyrene beads of 2.17 μm diameter (Spherotech) for 15 minutes. Then the mixture was diluted with 1 mL PBS and injected into the top channel of a microfluidic chamber (for further details on the microfluidics, please see [29]). Streptavidin-coated beads of 1.86 μm diameter were injected into the bottom channel of the chamber. Both bottom and top channels were connected to a central channel by capillary tubes. The beads were trapped in the central channel by sequentially approaching the top and bottom capillary tubes, out of which flowed a steady stream of anti-digoxigenin and streptavidin beads, respectively. Once one of each bead was trapped, a single SNARE complex was tethered between them by bringing the two beads close. The tethered molecule was pulled and relaxed by increasing or decreasing the trap separation at 10 nm/s, respectively, or held at a constant average force by keeping the trap separation constant. The optical tweezers experiment was conducted in PBS at 23 (±1) °C. To prevent oxidative photodamage by the strong trapping beams, we supplemented the PBS buffer with an oxygen scavenging, as described elsewhere [29].

Data Analysis

The data analysis to derive the intermediate structures and energies was performed as described in detail elsewhere [35]. Briefly, we obtained extension trajectories of folding/unfolding transitions at stepwise constant average forces by holding the protein at constant trap separations. The trajectories were mean-filtered to a bandwidth of 200 Hz or 1 kHz. We calculated the histogram distribution of the extension trajectories and determined the number of states by fitting the distribution with multiple-Gaussian functions. We then determined the state populations and transition rates, along with the state extensions and forces, using hidden Markov modeling (HMM) [34]. The idealized, noise-free trajectories were calculated using the Viterbi algorithm [42].

We calculated the state structures and energies at zero force by fitting the HMM-derived observables with a non-linear model. In this model, we chose the contour length of the unfolded, stretched portion of the protein L as the reaction coordinate to describe unfolding of the SNAREs along a pathway inferred from the crystal structure of the fully assembled SNARE complex [9]. Unfolding along the inferred pathway occurs by peeling off of the protein from the coiled-coil structure, starting from the C-terminus, while leaving the remaining, folded structure unperturbed (for more details, see [35]). To derive the conformations and free energies of folded, unfolded, and transition states, we defined a simplified energy landscape (L_i, V_i), where L_i is the contour length of the unfolded peptide in the i-th state and V_i the associated free energy at zero force. The (L_i, V_i) were determined by fitting the HMM-derived observables with a model that relates the experimental observables to the simplified energy landscape. The model expresses the mean extension of the i-th state, X_i, as

$$X_i = x^{(m)}(F_i, L) + H(F_i, L_i) + x^{(DNA)}(F_i), \quad (1)$$

where $x^{(m)}$ is the extension of the unfolded, stretched polypeptide, H is the extension of the folded, structured portion of the protein, $x^{(DNA)}$ is the extension of the DNA handle, and F_i is the mean state force. The extensions $x^{(m)}$ and $x^{(DNA)}$ are implicitly defined in terms of state force F_i, using the Marko-Siggia formula for the worm-like chain:

$$F_i = \frac{k_B T}{P}\left[\frac{1}{4\left(1 - \frac{x}{L}\right)^2} + \frac{x}{L} - \frac{1}{4}\right], \quad (2)$$

where P and L are the persistence length and contour length of the polymer, respectively. For DNA, we adopt $P_{DNA} = 40nm$ and $L_{DNA} = 0.34\frac{nm}{bp} \times 2260bp = 768.4nm$ for a 2,260 bp DNA handle. For polypeptide, we use $P_m = 0.6nm$ and $L = L_i$. We calculated the extension of the folded protein portion H using the freely jointed chain model

$$H_i = -\frac{k_B T}{F_i} + h(L_i)\coth\left(\frac{F_i h(L_i)}{k_B T}\right), \quad (3)$$

where $h(L_i)$ is the size of the structured portion of the protein along the pulling direction. The functional dependence of this core size h on the contour length L was directly determined from the protein crystal structure. A further constraint on the model is given by the relation of the trap separation D to the tether extension X_i, i.e.

$$D = X_i + \frac{F_i}{k_{traps}} + r_{strep} + r_{adig}, \quad (4)$$

where F_i / k_{traps} is the total displacement of the two beads from the traps, $k_{traps} = k_1 k_2 / (k_1 + k_2)$ is the effective stiffness of the two traps, and $r_{strep} + r_{adig}$ the sum of the bead radii. We get the state force at trap separation D by substituting Eqs. (1) to (3) into Eq. (4) and solving for F_i. Consequently, we also get the state extension X_i for a given state contour length L_i by plugging the calculated state force into Eq. (1).

The state populations and transition rates are determined from the free energy differences between the states. The free energies G_i are calculated as the sum

$$G_i = G^{(DNA)}(F_i) + G^{(m)}(F_i, L_i) + \frac{F_i^2}{2k_{traps}} + G^{(h)}(F_i, L_i) + V_i, \tag{5}$$

where $G^{(DNA)}$ and $G^{(m)}$ are the elastic energies of the DNA handle and unfolded polypeptide, $F_i^2 / 2k_{traps}$ is the potential energy of the trapped beads, $G^{(h)}$ is the entropic energy of the structured protein that arises from rotational degrees of freedom, and V_i is the intrinsic, force-independent free energy of the protein, which is unknown and thus set as a fitting parameter. The elastic energies $G^{(DNA)}$ and $G^{(m)}$ are given by the worm-like chain model as

$$G^{(m/DNA)} = \frac{k_B T}{P} \frac{L}{4\left(1 - \frac{x}{L}\right)} \left[3\left(\frac{x}{L}\right)^2 - 2\left(\frac{x}{L}\right)^3 \right]. \tag{6}$$

Similarly, the entropic, rotational energy of the structured core is given as

$$G_i^{(h)} = k_B T \left\{ -1 + \frac{Fh(L_i)}{k_B T} \coth\left(\frac{Fh(L_i)}{k_B T}\right) + \ln\left[\frac{\frac{Fh(L_i)}{k_B T}}{\sinh\left(\frac{Fh(L_i)}{k_B T}\right)} \right] \right\} . \tag{7}$$

With the state energies G_i defined, we can calculate the state populations P_i using the Boltzmann distribution, i.e.

$$P_i = \frac{e^{-\frac{G_i}{k_B T}}}{e^{-\frac{G_f}{k_B T}} + e^{-\frac{G_u}{k_B T}}}, \quad (8)$$

where G_f and G_u are the system energies for the folded and unfolded states, respectively. Additionally, we can calculate the folding and unfolding rates k_f and k_u, respectively, using Kramers' equation

$$k_f = k_m e^{-\frac{G^\dagger - G_u}{k_B T}} \quad (9)$$

and

$$k_u = k_m e^{-\frac{G^\dagger - G_f}{k_B T}}, \quad (10)$$

where $G^\dagger$ is the system energy of the transition state, and the pre-factor k_m is the diffusion-limited rate constant in the absence of an energy barrier. We adopted $k_m = 10^6 s^{-1}$, consistent with the fastest folding speeds observed for short helical proteins.

Last, we used non-linear least-squares method to fit the HMM-derived mean state extensions and forces, as well as the state populations and transition rates at all experimental trap separations with the model-based calculations, while using the state contour lengths and protein free energies at zero force as fitting parameters. The resulting best-fit parameters yield the simplified energy landscape at zero force that defines the energetics, kinetics, and state structures of the two-state transition. For the ternary SNARE complex, we evaluated the NTD, CTD, and

LD separately, where applicable. The full assembly energy landscape was then compiled from the individual transitions.

AUTHOR CONTRIBUTIONS

A.A.R, L.M, S.K, J.E.R, and Y.Z. designed the experiments. A.A.R, B.W, L.M, Q.H., S.M.A., and J.C. performed the experiments. A.A.R, B.W, S.K., J.E.R., and Y.Z. analyzed and interpreted the data. A.A.R, S.K., J.E.R, and Y.Z., wrote the article.

ACKNOWLEDGEMENTS

This work was supported by the NIH grants F31GM119312 to A. R., R01GM093341 and R01GM120193 to Y. Z., and R01DK027044 to J. E. R. We acknowledge support from the Raymond and Beverly Sackler Institute for Biological, Physical, and Engineering Sciences at Yale.

FIGURE LEGENDS

FIGURE 1 SNARE complex and experimental setup. The ternary SNARE complex forms a parallel four-helix bundle that is stabilized by inward-facing residues in layers -8 to +8. Engineered cysteines at the -6 layer create a disulfide bridge between syntaxin and VAMP2 to facilitate SNARE re-assembly. SNARE assembly occurs by sequential folding of the N-terminal domain (NTD), the C-terminal domain (CTD), and the linker domain (LD). The N-terminal Habc domain in syntaxin recruits other proteins to regulate SNARE assembly [43, 44], but minimally affects ternary SNARE assembly in the absence of these regulatory proteins in our assay [15]. Disease-causing mutations SNAP-25B I67T and I67N disrupt the hydrophobic contacts in the +4 layer.

FIGURE 2 SNAP-25B mutations destabilize SNARE CTD. (a) Force-extension curves (FECs) obtained by pulling (black) or relaxing (cyan) single SNARE complexes. SNARE complexes. Different SNARE folding states are marked by red numbers of states depicted in b. These states are derived from continuous regions in the FECs (red solid curves) or regions with discrete but distinct extensions (red dashed lines) based on the worm-like chain model [32]. (b) Diagrams of different SNARE folding states. The folding states of the WT SNARE complex include the fully assembled SNARE state (state 1), the LD-unfolded four-helix bundle state (2), the partially zippered state (3), the unzipped state (4), and the fully unfolded state (5). Folding of both SNARE complexes containing SNAP-25B mutations bypasses the state 2.

FIGURE 3 Representative extension-time trajectories containing the LD/CTD transition for I67T and I67N or the CTD transition for WT. The mean force F was kept constant for each trajectory by fixing the distance between two optical traps. Red traces represent idealized state trajectories as determined by hidden Markov Modeling (HMM). Double-Gaussian fits (green) of the extension probability density distributions reveal transitions between the two discrete states indicated by their corresponding state numbers (Fig. 2b). All extension traces share the same length and time scale bars, except for the trace at the bottom, which has a different time scale bar for a close-up view.

FIGURE 4 Zippering energy and kinetics of WT and mutant SNARE complexes. (a, b) Force-dependent unfolding probabilities (top panel) and transition rates (bottom panel) for CTD and LD/CTD transitions (a) or NTD transitions (b). Symbols denote measurements from time-extension trajectories for CTD transition in WT (black circles) and LD/CTD transition in I67T (red diamonds) or I67N (blue squares). Folding and unfolding rates are shown as hollow and solid symbols, respectively. Curves represent fitting results with a non-linear two-state model. (c) Comparison of NTD (gray) and LD/CTD (red) zippering energies between WT and mutant SNARE complexes. (d) Simplified energy landscape of SNARE zippering at zero force. The abscissa denotes the VAMP2 residue to which the SNARE complex is structured starting from the crosslinking site at -6 layer (residue 36). The regions corresponding to NTD, CTD, and LD are marked at the top of the graph. The derived stable and transition states are denoted by solid and hollow symbols, respectively. Solid lines denote an arbitrary interpolation between the calculated states to guide the eye.

FIGURE 5 Structures and dynamics of WT and mutant t-SNARE complexes. (a) The correctly folded t-SNARE complex (state iii) is prepared by completely unfolding a ternary SNARE complex (state i) *in situ* at high force and subsequent refolding the remaining t-SNAREs (state ii). Note that SNAP-25B contains an N-terminal SNARE domain (SN1) and a C-terminal SNARE domain (SN2) connected by a disordered linker. The t-SNARE complex is pulled from the C-termini of syntaxin and SN1. (b) FECs obtained by pulling t-SNARE complexes in ternary SNARE complexes (black) and then relaxing the t-SNARE complexes alone (cyan). Green arrows indicate LD/CTD transitions in ternary SNARE complexes. (c) Representative extension-time trajectories for the t-SNARE folding/unfolding transition near equilibrium force. Double-Gaussian fits (green) of the extension histogram distributions confirm the two-state nature of the transition. Red traces represent idealized state trajectories as determined by HMM.

FIGURE 6 Folding energies, kinetics, and conformations of t-SNARE complexes. (a) Force-dependent unfolding probabilities (top panel) and transition rates (bottom panel) of the t-SNARE complex. Symbols denote experimental measurements for WT (black circles), I67T (red diamonds), and I67N (blue squares). Folding and unfolding rates are shown as hollow and solid symbols, respectively. Best-fits with a two-state model are shown as curves. (b) Comparison of t-SNARE folding energies between WT and mutant complexes. (c) Simplified folding energy landscapes for t-SNARE complexes. The abscissa denotes the syntaxin residue to which the t-SNARE complex is structured starting from the crosslinking site at -8 layer (residue 199). Locations of corresponding hydrophobic and ionic layers are marked on top of the graph. The derived stable and transition states are shown as solid and hollow symbols, respectively, for WT (black), I67T (red), and I67N (blue).

REFERENCES

[1] Sudhof TC, Rothman JE. Membrane fusion: grappling with SNARE and SM proteins. Science. 2009;323:474-7.

[2] Weber T, Zemelman BV, McNew JA, Westermann B, Gmachl M, Parlati F, et al. SNAREpins: Minimal machinery for membrane fusion. Cell. 1998;92:759-72.

[3] Sollner T, Whiteheart SW, Brunner M, Erdjument-Bromage H, Geromanos S, Tempst P, et al. SNAP receptors implicated in vesicle targeting and fusion. Nature. 1993;362:318-24.

[4] Bennett MK, Calakos N, Scheller RH. Syntaxin - a synaptic protein implicated in docking of synaptic vesicles at presynaptic active zones. Science. 1992;257:255-9.

[5] Trimble WS, Cowan DM, Scheller RH. VAMP-1 - a synaptic vesicle-associated integral membrane-protein. Proc Natl Acad Sci USA. 1988;85:4538-42.

[6] Baumert M, Maycox PR, Navone F, Decamilli P, Jahn R. Synaptobrevin - an integral membrane-protein of 18000 daltons present in small synaptic vesicles of rat-brain. EMBO J. 1989;8:379-84.

[7] Sudhof TC, Baumert M, Perin MS, Jahn R. A synaptic vesicle membrane-protein is conserved from mammals to Drosophila. Neuron. 1989;2:1475-81.

[8] Oyler GA, Higgins GA, Hart RA, Battenberg E, Billingsley M, Bloom FE, et al. The identification of a novel synaptosomal-associated protein, SNAP-25, differentially expressed by neuronal subpopulations. J Cell Biol. 1989;109:3039-52.

[9] Sutton RB, Fasshauer D, Jahn R, Brunger AT. Crystal structure of a SNARE complex involved in synaptic exocytosis at 2.4 angstrom resolution. Nature. 1998;395:347-53.

[10] Sorensen JB, Wiederhold K, Muller EM, Milosevic I, Nagy G, de Groot BL, et al. Sequential N- to C-terminal SNARE complex assembly drives priming and fusion of secretory vesicles. EMBO J. 2006;25:955-66.

[11] Pobbati AV, Stein A, Fasshauer D. N- to C-terminal SNARE complex assembly promotes rapid membrane fusion. Science. 2006;313:673-6.

[12] Gao Y, Zorman S, Gundersen G, Xi ZQ, Ma L, Sirinakis G, et al. Single reconstituted neuronal SNARE complexes zipper in three distinct stages. Science. 2012;337:1340-3.

[13] Fasshauer D, Sutton RB, Brunger AT, Jahn R. Conserved structural features of the synaptic fusion complex: SNARE proteins reclassified as Q- and R-SNAREs. Proc Natl Acad Sci USA. 1998;95:15781-6.

[14] Walter AM, Wiederhold K, Bruns D, Fasshauer D, Sorensen JB. Synaptobrevin N-terminally bound to syntaxin-SNAP-25 defines the primed vesicle state in regulated exocytosis. J Cell Biol. 2010;188:401-13.

[15] Ma L, Rebane AA, Yang G, Xi Z, Kang Y, Gao Y, et al. Munc18-1-regulated stage-wise SNARE assembly underlying synaptic exocytosis. eLIFE. 2015;4:e09580.

[16] Jeans AF, Oliver PL, Johnson R, Capogna M, Vikman J, Molnar Z, et al. A dominant mutation in SNAP25 causes impaired vesicle trafficking, sensorimotor gating, and ataxia in the blind-drunk mouse. Proc Natl Acad Sci USA. 2007;104:2431-6.

[17] Garcia-Reitbock P, Anichtchik O, Bellucci A, Iovino M, Ballini C, Fineberg E, et al. SNARE protein redistribution and synaptic failure in a transgenic mouse model of Parkinson's disease. Brain. 2010;133:2032-44.

[18] Johnson RD, Oliver PL, Davies KE. SNARE proteins and schizophrenia: linking synaptic and neurodevelopmental hypotheses. Acta Biochim Pol. 2008;55:619-28.

[19] Spessott WA, Sanmillan ML, McCormick ME, Kulkarni VV, Giraudo CG. SM protein Munc18-2 facilitates transition of Syntaxin 11-mediated lipid mixing to complete fusion for T-lymphocyte cytotoxicity. Proc Natl Acad Sci USA. 2017;114:E2176-E85.
[20] Stockli J, Fazakerley DJ, James DE. GLUT4 exocytosis. J Cell Sci. 2011;124:4147-58.
[21] Shen XM, Selcen D, Brengman J, Engel AG. Mutant SNAP25B causes myasthenia, cortical hyperexcitability, ataxia, and intellectual disability. Neurology. 2014;83:2247-55.
[22] Engel AG, Shen XM, Selcen D, Sine SM. Congenital myasthenic syndromes: pathogenesis, diagnosis, and treatment. Lancet Neurol. 2015;14:420-34.
[23] Avdoshenko SM, Makarov DE. Reaction Coordinates and Pathways of Mechanochemical Transformations. J Phys Chem B. 2016;120:1537-45.
[24] Weninger K, Bowen ME, Chu S, Brunger AT. Single-molecule studies of SNARE complex assembly reveal parallel and antiparallel configurations. Proc Natl Acad Sci USA. 2003;100:14800-5.
[25] Zhang YL. Energetics, kinetics, and pathway of SNARE folding and assembly revealed by optical tweezers. Protein Sci. 2017;26:1252-65.
[26] Bustamante C, Chemla YR, Forde NR, Izhaky D. Mechanical processes in biochemistry. Annu Rev Biochem. 2004;73:705-48.
[27] Sirinakis G, Ren YX, Gao Y, Xi ZQ, Zhang YL. Combined and versatile high-resolution optical tweezers and single-molecule fluorescence microscopy. Rev Sci Instrum. 2012;83:093708.
[28] Moffitt JR, Chemla YR, Izhaky D, Bustamante C. Differential detection of dual traps improves the spatial resolution of optical tweezers. Proc Natl Acad Sci USA. 2006;103:9006-11.
[29] Jiao JY, Rebane AA, Ma L, Zhang YL. Single-molecule protein folding experiments using high-resolution optical tweezers. Methods Mol Biol. 2017;1486:357-90.
[30] Zorman S, Rebane AA, Ma L, Yang GC, Molski MA, Coleman J, et al. Common intermediates and kinetics, but different energetics, in the assembly of SNARE proteins. Elife. 2014;3:e03348.
[31] Cecconi C, Shank EA, Bustamante C, Marqusee S. Direct observation of the three-state folding of a single protein molecule. Science. 2005;309:2057-60.
[32] Bustamante C, Marko JF, Siggia ED, Smith S. Entropic elasticity of lambda-phage DNA. Science. 1994;265:1599-600.
[33] Liphardt J, Onoa B, Smith SB, Tinoco I, Bustamante C. Reversible unfolding of single RNA molecules by mechanical force. Science. 2001;292:733-7.
[34] Zhang YL, Jiao J, Rebane AA. Hidden Markov modeling with detailed balance and its application to single protein folding Biophys J. 2016;111:2110-24.
[35] Rebane AA, Ma L, Zhang YL. Structure-based derivation of protein folding intermediates and energies from optical tweezers. Biophys J. 2016;110:441-54.
[36] Jackson SE, Fersht AR. Folding of Chymotrypsin Inhibitor-2 .1. Evidence for a 2-State Transition. Biochemistry-Us. 1991;30:10428-35.
[37] Guinn EJ, Jagannathan B, Marqusee S. Single-molecule chemo-mechanical unfolding reveals multiple transition state barriers in a small single-domain protein. Nat Commun. 2015;6.
[38] Zhang XM, Rebane AA, Ma L, Li F, Jiao J, Qu H, et al. Stability, folding dynamics, and long-range conformational transition of the synaptic t-SNARE complex. Proc Natl Acad Sci USA. 2016;113:E8031-E40.
[39] Mohrmann R, de Wit H, Verhage M, Neher E, Sorensen JB. Fast vesicle fusion in living cells requires at least three SNARE complexes. Science. 2010;330:502-5.

[40] Shi L, Shen QT, Kiel A, Wang J, Wang HW, Melia TJ, et al. SNARE proteins: One to fuse and three to keep the nascent fusion pore open. Science. 2012;335:1355-9.
[41] Gittes F, Schmidt CF. Interference model for back-focal-plane displacement detection in optical tweezers. Optics Letters. 1998;23:7-9.
[42] Viterbi AJ. Error bounds for convolutional codes and an asymptotically optimum decoding algorithm. Ieee T Inform Theory. 1967;13:260-9.
[43] Fernandez I, Ubach J, Dulubova I, Zhang XY, Sudhof TC, Rizo J. Three-dimensional structure of an evolutionarily conserved N-terminal domain of syntaxin 1A. Cell. 1998;94:841-9.
[44] Shen JS, Tareste DC, Paumet F, Rothman JE, Melia TJ. Selective activation of cognate SNAREpins by Sec1/Munc18 proteins. Cell. 2007;128:183-95.

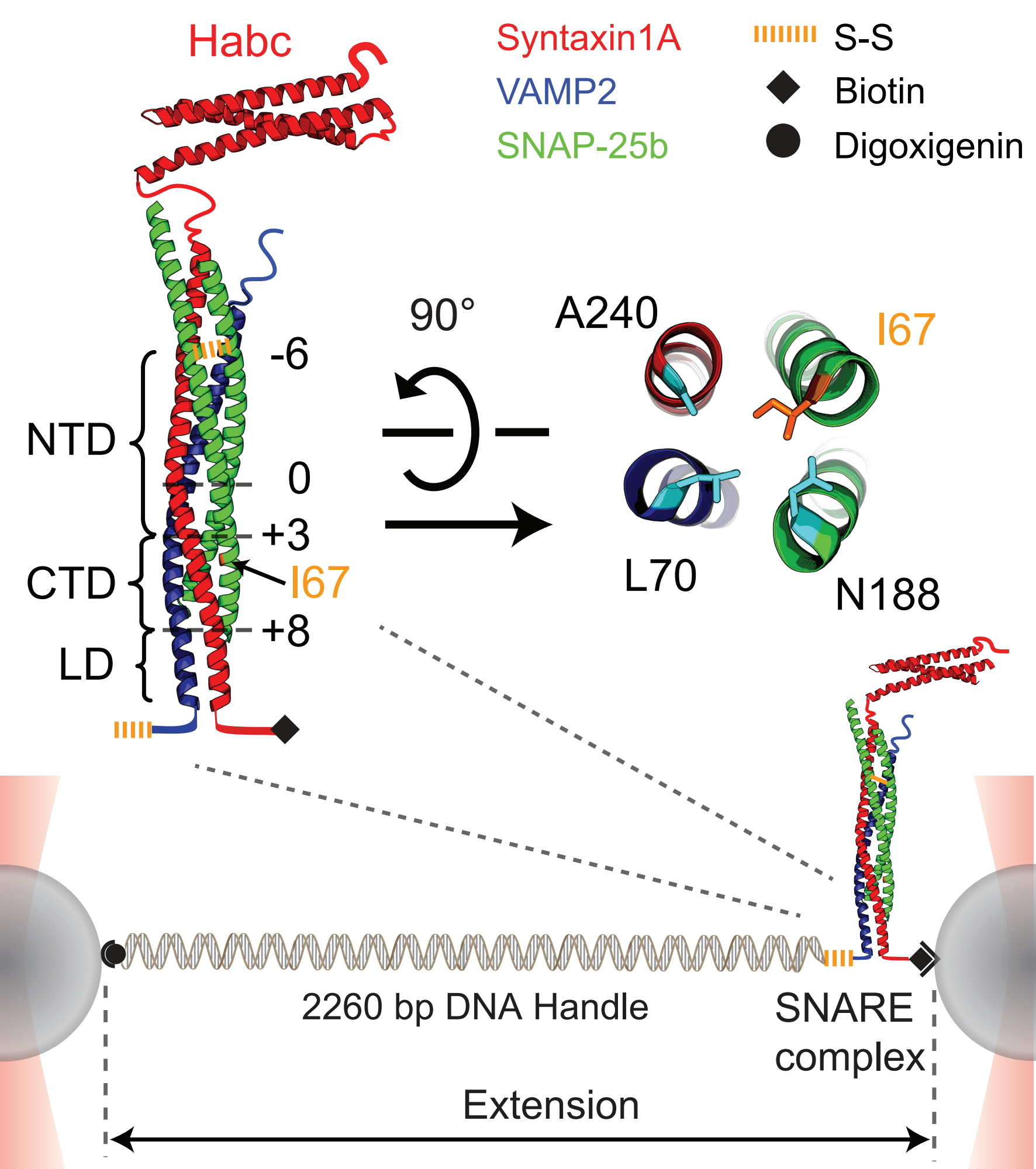
Habc
Syntaxin1A
VAMP2
SNAP-25b
S-S
Biotin
Digoxigenin
90°
A240
I67
L70
N188
-6
0
+3
+8
NTD
CTD
LD
I67
2260 bp DNA Handle
SNARE complex
Extension

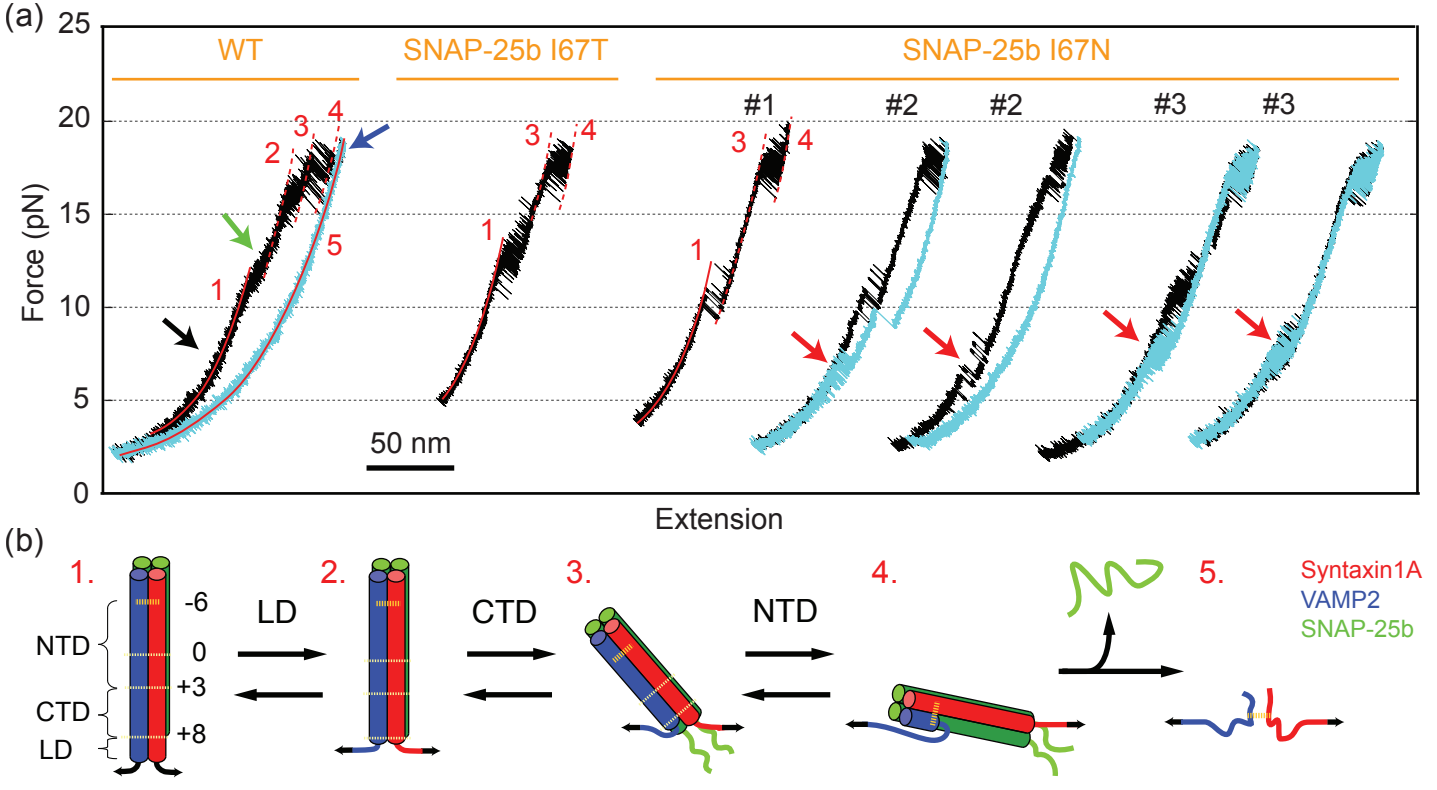
(a)
WT
SNAP-25b I67T
SNAP-25b I67N
#1
#2
#2
#3
#3
Force (pN)
Extension
50 nm
(b)
1.
2.
3.
4.
5.
NTD
CTD
LD
-6
0
+3
+8
LD
CTD
NTD
Syntaxin1A
VAMP2
SNAP-25b

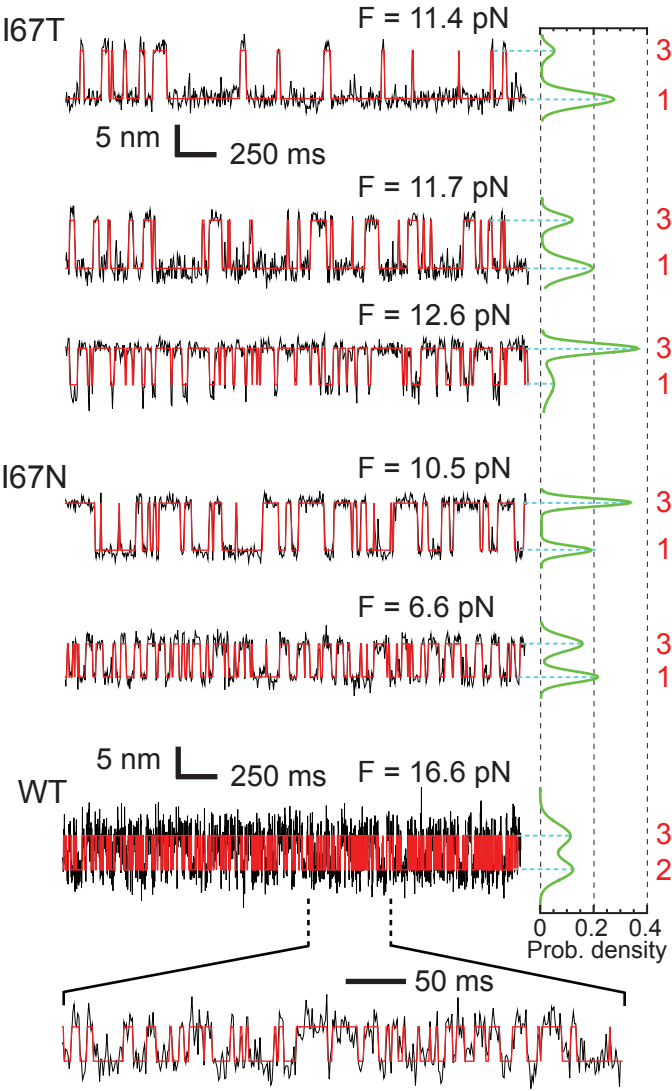
I67T
F = 11.4 pN
3
1
5 nm
250 ms
F = 11.7 pN
3
1
F = 12.6 pN
3
1
I67N
F = 10.5 pN
3
1
F = 6.6 pN
3
1
5 nm
250 ms
WT
F = 16.6 pN
3
2
0
0.2
0.4
Prob. density
50 ms

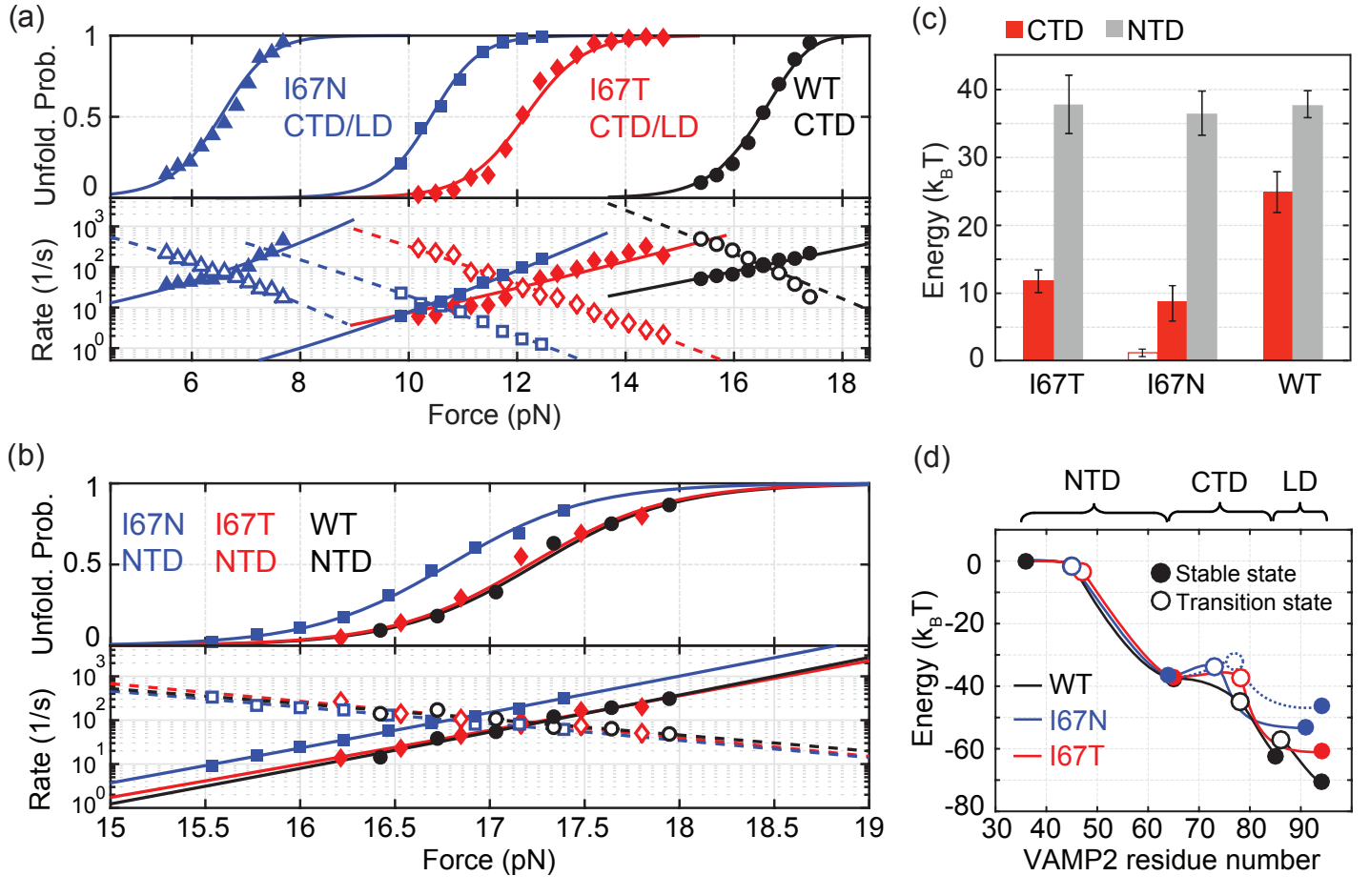
(a)
Unfold. Prob.
I67N
CTD/LD
I67T
CTD/LD
WT
CTD
Rate (1/s)
Force (pN)
(b)
Unfold. Prob.
I67N
NTD
I67T
NTD
WT
NTD
Rate (1/s)
Force (pN)
(c)
CTD
NTD
Energy (k_BT)
I67T
I67N
WT
(d)
NTD
CTD
LD
Stable state
Transition state
WT
I67N
I67T
Energy (k_BT)
VAMP2 residue number

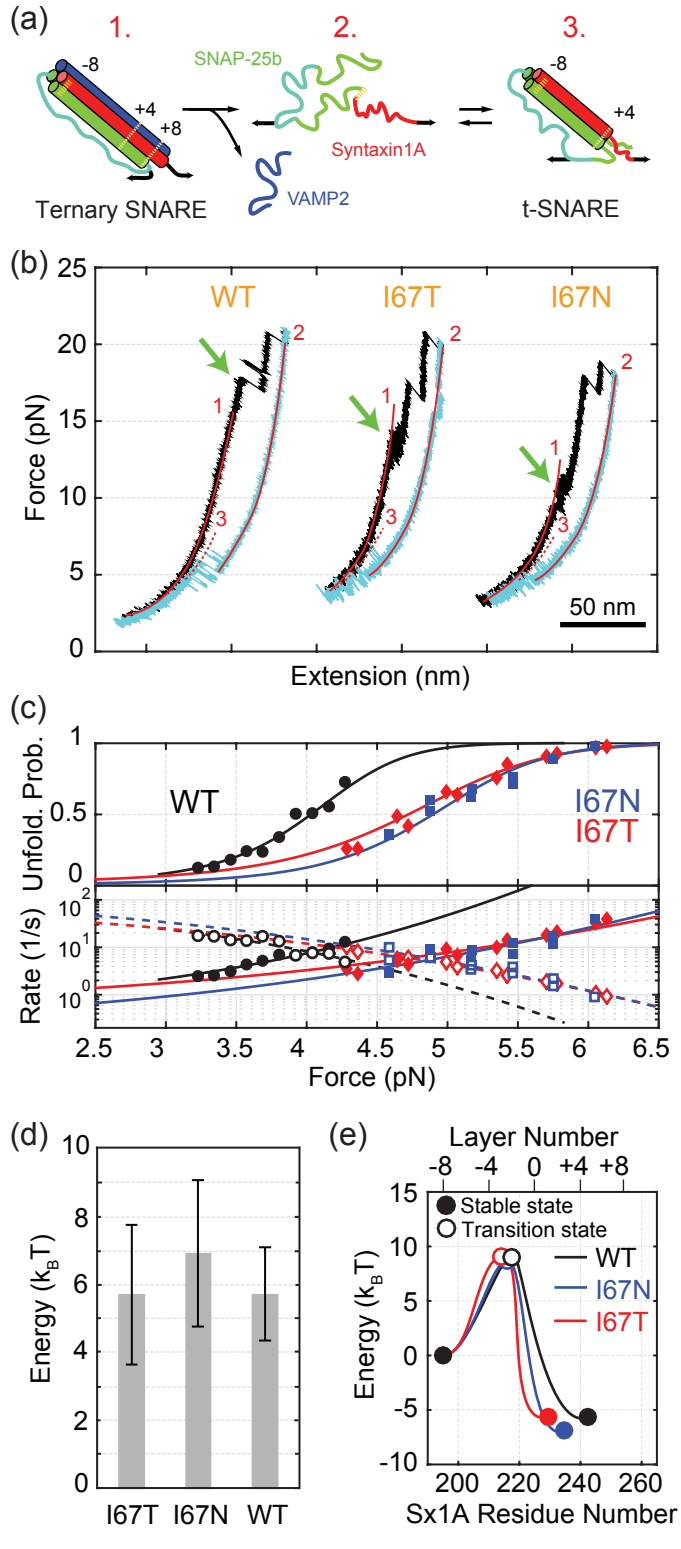
(a)
1.
2.
3.
-8
+4
+8
SNAP-25b
Syntaxin1A
VAMP2
Ternary SNARE
t-SNARE
(b)
WT
I67T
I67N
Force (pN)
Extension (nm)
50 nm
(c)
Unfold. Prob.
WT
I67N
I67T
Rate (1/s)
Force (pN)
(d)
Energy (k_BT)
I67T
I67N
WT
(e)
Layer Number
Stable state
Transition state
WT
I67N
I67T
Energy (k_BT)
Sx1A Residue Number